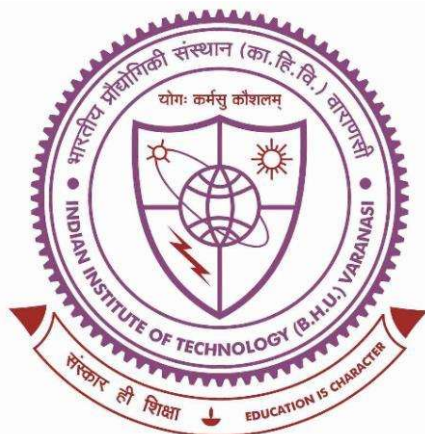


Electron Microscopy of Interfaces in Au/Cu Multilayer on Si, Li(Ni,Mn)_xO_y on Nb-doped SrTiO₃ and Nanocomposite Steel



**Thesis submitted in partial fulfilment for the
Award of Degree**

Doctor of Philosophy

By

Ankit Singh

**DEPARTMENT OF METALLURGICAL ENGINEERING
INDIAN INSTITUTE OF TECHNOLOGY
(BANARAS HINDU UNIVERSITY)
VARANASI – 221005
INDIA**

Roll No. 15141001

2022

CERTIFICATE

It is certified that the work contained in the thesis titled “**Electron microscopy of interfaces in Au/Cu Multilayer on Si, Li(Ni,Mn)_xO_y on Nb-doped SrTiO₃ and Nanocomposite Steel**” by **Ankit Singh** has been carried out under our joint supervision and this work has not been submitted elsewhere for a degree.

It is further certified that the student has fulfilled all the requirements of Comprehensive, Candidacy and SOTA for the award of Ph.D. degree.



13-06-2022

Prof. R.K. Mandal
(Supervisor)
Professor

Department of Metallurgical Engineering
Indian Institute of Technology
(Banaras Hindu University)
Varanasi



13-06-2022

Dr. Joysurya Basu
(Co-Supervisor)
Associate Professor


Department of Metallurgical Engineering
Indian Institute of Technology
(Banaras Hindu University)
Varanasi

DECLARATION BY THE CANDIDATE

I, **Ankit Singh**, certify that the work embodied in this Ph.D. thesis is my own bonafide work carried out by me under the joint supervision of **Prof. Rajiv Kumar Mandal** and **Dr. Joysurya Basu** for a period from **July 2015** to **June 2022** at the “**Department of Metallurgical Engineering**”, Indian Institute of Technology (BHU), Varanasi, India. The matter embodied in this Ph.D. thesis has not been submitted for the award of any other degree/diploma. I declare that I have faithfully acknowledged and given credits to the research workers wherever their works have been cited in my work in this thesis. I further declare that I have not willfully copied any other's work, paragraphs, text, data, results, etc., reported in journals, books, magazines, reports dissertations, thesis, etc., or available at websites and have not included them in this thesis and have not cited as my own work.

Date: 13-06-2022

Place: Varanasi



(ANKIT SINGH)

CERTIFICATE BY THE SUPERVISORS

This is to certify that the above statement made by the candidate is correct to the best of our knowledge.



13-06-2022

Prof. R.K. Mandal

(Supervisor)

Professor

Department of Metallurgical Engineering
Indian Institute of Technology
(Banaras Hindu University)
Varanasi



13-06-2022

Dr. Joysurya Basu

(Co-Supervisor)

Associate Professor

Department of Metallurgical Engineering
Indian Institute of Technology
(Banaras Hindu University)
Varanasi

Forwarded by:



Prof. Sumil Mohan
(Head of Department)

Department of Metallurgical Engineering
Indian Institute of Technology
(Banaras Hindu University)
Varanasi – 221005, India

COPYRIGHT TRANSFER CERTIFICATE

Title of the Thesis: Electron microscopy of interfaces in Au/Cu Multilayer on Si, Li(Ni,Mn)_xO_y on Nb-doped SrTiO₃ and Nanocomposite Steel.



Candidate's name : Ankit Singh

COPYRIGHT TRANSFER

The undersigned hereby assigns to the Indian Institute of Technology (Banaras Hindu University), Varanasi all rights under copyright that may exist in and for the above thesis submitted for the award of the *Doctor of Philosophy*.

Date: 13-06-2022

Place: Varanasi



(Ankit Singh)

Note: However, the author may reproduce or authorize others to reproduce materials extracted verbatim from the thesis or derivative of the thesis for author's personal use provided that the source and the Institute's copyright notice are indicated.

ACKNOWLEDGEMENT

At the onset, I take the opportunity to offer this endeavour to almighty God for the wisdom he bestowed upon me to finish this research.

I would like to express my sincere gratitude and special thanks to my supervisors Prof. R K Mandal, and Dr. Joysurya Basu, for imparting their knowledge and expertise in this study. I consider myself very fortunate to have learnt the basics of solid state phase transformations and crystallography from Prof. R.K. Mandal. His exceptional understanding towards these subjects and their applicability have made me to adopt an independent way of conceiving the concepts. He has always inspired me to emphasise quality in the work rather than quantity, which immensely benefited me. In simple words, I would say, he is a “Man of simple living and high thinking”. I am extremely thankful to him for the critical suggestions he proposed in his inimitable style for the improvement of the thesis. I would always appreciate his exemplary noble behaviour and systematic way of working. It is great experience working under his guidance.

It is my privilege to express by sense of gratitude to Dr. Joysurya Basu, for training me on the transmission electron microscope and introducing me with the advanced electron microscopy techniques such as In-situ TEM, cross-section TEM sample preparation, EELs, etc. In addition, he has taught me several topics related to electron diffraction and image simulation. His exceptional experimental skills and analytical capabilities helped me, particularly in executing my work. His untiring and selfless approach towards research has always strengthened my research aptitude. I have acquired the quality of being positive and patient from him in all ups and downs. His ability of listening to my silliest query and turning it into a logical one has always boosted up my confidence. His approach of putting the complex things in a simple and clear manner has always inspired me to keep perfection in my work. I am indebted to him for inspiring guidance, unstinted support and persistent encouragement throughout the course of this work.

Beside my supervisors, I would also like to convey my thanks to Prof. S. Lele, Prof. GVS Sastry and Prof. N K Mukhopadhyaya for fruitful discussions and, former heads of department for their kind support. I thank Prof. Sunil Mohan, the current head of department for his invaluable contribution.

I am grateful to the other faculty members of IIT BHU for their encouragement and support. I would also like to express my gratitude to the entire non-teaching staff of the Metallurgical Engineering Department of IIT BHU.

I sincerely thank Prof. S. Jit, Electronics Engineering, IIT (BHU), for extending the thermal evaporation facility. My special thanks to Dr. Sandip Bysakh, CGCRI, Kolkata for extending the required experimental facilities in preparing cross-section TEM specimens of Au/Cu multilayer thin films. I would also thank Dr. Vishwanath Balakrishnan, for extending the facilities for the preparation of amorphous-steel cross-section specimens. I gratefully acknowledge Dr. Imteyaz Ahmed, Ceramic Engineering, IIT (BHU), for availing the fume hood facility. It is my pleasure to thank Dr. Leonid A. Bendersky, NIST, USA, for providing the TEM sample preparation facility. My hearty thanks to Dr. T. Ichiro, for pulsed laser deposition facility, I am also thankful to Dr. Shintaro for his experimental support. I am extremely thankful to the Tata Steel, Jamshedpur team Dr. Manojit Dutta, Dr. Atanu Banerjee and Mr. Pavan Bijalwan, for getting the thermal spraying, SEM, and ball milling done. Working with them have been great learning process through various scientific discussion.

I would also like to thank EMSI, Research & Development (IIT BHU), Mrs. Indira Anathachari endowment fund, and IIM Trust for extending me financial assistance for attending the national and international Conferences.

I am grateful to my present and former labmates, Dr. Manish Singh, Dr. Vikas Shivam, Dr. Raj Bahadur, Dr. Vivek Pandey, Dr. Yagnesh Shadangi, Dr. Rajendra Gore, Dr. Arunabh, Dr. Raj, Dr. Ch. Rao, Avnish, Asnit, Aman, Shubham, Roopchand, Saarika, Soham, Saptarishi, Satyam, Sandeep, Debabrata, Shravan, Harsh, and colleagues Amit, Akansha, Ankur, and Mamta, for their fruitful discussion about science and keeping cheerful atmosphere to work.

At personal front, I wish to express my sincere gratitude and indebtedness to my parents Mr. Arvind Singh and Mrs. Kanak Singh for their blessings, care, and support. I would also like to thank Ankur, Mamta, Akanksha and Amit for their cheerful company

Finally, I am extremely thankful to Mrs. Shivangi Singh (wife), and Mrs. Poonam Singh (mother-in-law) for their constant encouragement and moral support throughout this journey.



13-06-2022 (Ankit Singh)

Table of Contents

Abbreviations.....	xix
CHAPTER-1	i
1.1 Surfaces and interfaces	1
1.2 Dynamics of surfaces/interfaces and microstructure evolution	3
1.2.1 Atomic level distortions	4
1.2.2 Wulff construction	6
1.2.3 Surface/interface coupling	7
1.2.4 Structural transformations and chemistry	9
1.3 Design of surfaces/interfaces	10
1.3.1 Technical importance	10
1.3.2 Stability and growth	11
1.3.3 Interfacial structure and properties	12
1.4 Surfaces/interfaces at various length scales	15
1.5 Classification of interfaces	15
1.6 Surfaces/Interfaces in nanostructured materials	16
1.7 TEM investigation of surfaces/ interfaces	18
1.7.1 Other techniques	19
1.7.1.1 Diffraction contrast imaging	20
1.7.1.2 Phase contrast imaging	21
1.7.1.3 Z-contrast imaging or HAADF-STEM	22
1.7.1.4 X-ray energy dispersive spectroscopy (XEDS)	23
1.7.1.5 Electron energy loss spectroscopy (EELS)	24
1.8 Multislice image simulations and structure modelling	25
1.9 Miedema model	26
1.10 Material dependent role of surfaces and interfaces	27
1.10.1 Metal/Metal heterophase interfaces in nanostructured multilayer thin films 27	
1.10.2 Ceramic/Ceramic heterophase interfaces in thin films	30
1.10.3 Glass/Metal interfaces in amorphous nanocomposites and thin films	31
1.11 Objectives of the thesis	32
2 CHAPTER-2	35
2.1 Materials systems	37
2.2 Materials synthesis	38
2.2.1 Thermal evaporation of Au/Cu multilayers	39

Table of Contents

2.2.2	Pulsed laser deposition of $\text{Li}(\text{Ni},\text{Mn})_x\text{O}_y/\text{Nb-SrTiO}_3$ thin films	41
2.2.3	Alloy preparation	42
2.2.4	Melt spinning.....	42
2.2.5	Ball milling.....	42
2.2.6	Thermal spraying (HVOF).....	43
2.3	Cross-section specimen preparation for TEM	43
2.3.1	Au/Cu multilayer thin films specimen preparation	44
2.3.2	LNMO/ Nb:STO core-shell thin films specimen preparation.....	46
2.3.3	Amorphous-steel nanocomposite/ mild steel coatings specimen preparation.....	47
2.4	Structural characterization	47
2.4.1	Grazing incidence X-ray diffraction.....	48
2.4.2	X-ray diffraction	49
2.4.3	Scanning electron microscopy (SEM)	49
2.4.4	Transmission electron microscopy (TEM).....	51
2.5	Computational techniques.....	54
2.5.1	XRD pattern simulation	54
2.5.2	MATLAB.....	55
3	CHAPTER-3.....	57
3.1	Introduction.....	59
3.2	Experimental procedure.....	61
3.2.1	Thin film deposition	61
3.2.2	Grazing incidence X-ray diffraction (GIXRD).....	62
3.2.3	TEM cross-section specimen preparation.....	62
3.2.4	Simulation of grazing incidence x-ray patterns and high resolution images..	63
3.3	Results	64
3.3.1	GIXRD and simulation	64
3.3.2	Diffraction contrast imaging, morphology and chemistry	70
3.3.3	Selected area diffraction (SAD)	73
3.3.4	High-resolution phase contrast imaging	74
3.3.4.1	Cu/Si interface and defects.....	75
3.3.4.2	Au/Cu interfaces and defects	79
3.3.5	Multislice simulation and direct structure imaging	87
3.4	Discussion.....	94
3.4.1	Phase evolution, growth morphology and kinetics.....	94
3.4.2	Amorphization at the interfaces and associated challenges	99

Table of Contents

3.4.3	Structure evolution of multilayer and interfaces	100
3.4.4	Metastability landscape of the Au-Cu phase diagram	105
3.5	Conclusions	107
4	CHAPTER-4	109
4.1	Introduction	111
4.2	Experimental methods	112
4.3	Results.....	112
4.4	Discussion	121
4.5	Conclusions	124
5	CHAPTER-5	127
5.1	Introduction	129
5.2	Experiments	132
5.2.1	Thin film deposition	132
5.2.2	Experimental electron microscopy.....	134
5.2.3	Multislice simulation and electron diffraction	134
5.3	Results.....	135
5.3.1	Electron diffraction and diffraction contrast imaging.....	135
5.3.2	Spectral imaging and composition analysis.....	144
5.3.3	Structural imaging and interfaces.....	146
5.4	Discussion	160
5.4.1	Microstructure, chemistry, phases and interfaces.....	160
5.4.2	Atomic origin of electro-chemical activity.....	164
5.4.3	Defects origin and mechanism.....	167
5.5	Conclusions	169
6	CHAPTER-6	171
6.1	Introduction	173
6.2	Experiments	175
6.2.1	Synthesis	175
6.2.2	Characterization	177
6.2.3	Multislice simulation and diffraction patterns.....	178
6.3	Results.....	179
6.3.1	X-ray diffraction.....	179
6.3.2	Mass-thickness and diffraction contrast imaging.....	186
6.3.3	Identification of the faceted nanocrystals in the amorphous coating	190

Table of Contents

6.3.4	Atomically resolved phase contrast imaging	192
6.4	Discussion.....	206
6.4.1	Phase evolution, local structure and polyhedral order	206
6.4.2	Statistical nature of precipitation, phase selection and chemistry.....	211
6.4.3	Complexities at the surfaces and interfaces.....	213
6.5	Relative thermodynamic stabilities	215
6.6	Conclusions.....	219
7	CHAPTER-7.....	171
7.1	Summary.....	223
7.1.1	Crystalline/crystalline interfaces in Au/Cu multilayer thin films.....	223
7.1.2	Crystalline/crystalline interfaces in LNMO/ Nb:STO thin film	224
7.1.3	Crystalline/amorphous interfaces in amorphous steel coatings and nanocomposites	225
7.2	Scope and suggestions for future work	225
8	References	221
9	List of publications.....	255
10	List of conference presentations	256

LIST OF FIGURES

Figure 1.1: Schematic representation of homophase surfaces/interfaces in the engineering materials **a)** grain boundary, **b)** twin boundary and, **c)** stacking fault.2

Figure 1.2: Schematic representation of heterophase surfaces/interfaces in the engineering materials [31].3

Figure 1.3: Interfacial dynamics at heterophase interfaces **a)** atomic relaxation, **b)** Surface atoms rearrangement, **c)** Strained interface, **d)** charge distribution at interface, **e)** distinct magnetic lines of forces at interfaces and, **f)** differently terminated interfaces.5

Figure 1.4: A schematic representation of Wulff construction for a cubic shape in 2D, where minimal surface energy for {100} planes are discerned.6

Figure 1.5: Description of the stability and growth of the heterophase surfaces and interfaces **a)** low strain state, **b)** high strain state, **c)** delocalized atomic bonds, and **d)** large difference in lattice fringes.12

Figure 1.6: Schematic representation of the complexities at the interfacial structure between material A and material B.13

Figure 1. 7: Schematic description of Au-Cu alloy nanoparticle in its two structural forms (cF4 and tP4) used as a catalyst for carbon monoxide (CO) oxidation. The tP4(AuCu) structure showed better catalytic activity than cF4 (AuCu) structure as Cu is less oxidized in the tP4 case15

Figure 1. 8: Classification of interfaces on the basis of **a)** states of matter, **b)** periodicity, **c)** length scale, **d)** engineering materials, **e)** conductivity, **f)** magnetism, **g)** bonding, **h)** coherency, and **i)** roughness.17

Figure 1.9: Two operating modes of TEM **a)** diffraction mode **b)** imaging mode20

Figure 1. 10: Schematic representation of **a)** HRTEM mode of operation **b)** STEM mode of operation23

Figure 1.11: Schematic of an electron beam with post column EELS and EDS detectors.24

Figure 1.12: Interfacial structures on the basis of coherency **a)** coherent, **b)** semi-coherent and, **c)** incoherent.28

Figure 1.13: Distinct types of interfacial structures, **a)** sharp, **b)** diffused and, **c)** Intermixed29

Figure 2.1: Schematic of a thermal evaporation chamber.39

List of Figures

Figure 2.2: Schematic of a pulsed laser deposition unit.	41
Figure 2.3: Schematic sequence for the Au/Cu multilayer (40TAu) cross-section specimen preparation. The same method is applied for the 40TCu specimen preparation, only the deposition sequence is reversed.....	45
Figure 2.4: Schematic sequence for the LNMO/ Nb:STO cross-section specimen preparation.	46
Figure 2.5: Schematic sequence for the cross-section specimen preparation of Fe-based amorphous/mild steel coatings.	46
Figure 2.6: Schematic of SEM a) Front half section, b) Electron beam trajectory [221].....	50
Figure 2.7: Schematic of a TEM a) overall cabinet assembly and, b) inside view.	53
Figure 2.8: Schematic representing path of an electron beam in TEM [221].	54
Figure 3.1: Phase diagram of Au-Cu system showing the existence of equilibrium solid solution phase above 410 °C along with intermetallics formation below this temperature over a wide composition range [104].	60
Figure 3.2: Experimental GIXRD pattern of multilayer Au/Cu thin film (Top in the multiple display). Enlarged version of the encircled region is given at the inset. Simulated patterns of possible Au-Cu phases with cF4, tP4, oI40, oP8 and cP4 structures are placed underneath for comparison.	65
Figure 3.3: a) TEM bright field image showing the cross-section view of Au/Cu multilayers along with the polycrystalline Si substrate. Individual Au and Cu layers along with the polycrystalline Si substrate has been marked b) X-ray energy dispersive spectrum (XEDS) and spectral map from the multilayer thin film. Extensive interdiffusion is observed across the interface of the multilayer. c) corresponding selected area electron diffraction pattern obtained from the Au/Cu multilayers only. Experimentally obtained d-spacings have been marked in the diffraction pattern.	71
Figure 3.4: a) Cross-section high magnification diffraction contrast image of Au/Cu multilayers representing the individual amorphous Cu layer and Au crystalline layer. Interface reactions and morphology, moire patterns and inter-columnar boundaries have also been indicated by arrows and dotted curves respectively. White arrows represent remnant strains during non-equilibrium solidification b) cross-section high-resolution phase contrast image of the film-substrate interface. Dotted	

curve indicates the reaction product of Cu-Si interface. Inset shows the SAD of Si grain oriented along [1 1 2] zone axis. **c)** cross-section high resolution phase contrast image of amorphous Cu/Si interface. Wavy dotted curve within the substrate demarcates the boundary beyond which lattice fringes disappear. Two different contrast regions marked by dotted squares named as ‘e’ and ‘f’ along with their corresponding FFTs (represented at the insets) and inverse FFTs as displayed in figure 3.4e and figure 3.4f respectively. **d)** High-resolution phase contrast image obtained from the region few nm inside the surface of the substrate showing Si clusters as indicated by arrows those are surrounded by amorphous Si. Corresponding FFTs obtained from the Si clusters are shown in the insets. Regions ‘x’ and ‘y’ within the amorphous Si as indicated by solid circles are cropped and shown separately in figure 3.4X and figure 3.4Y respectively. Amorphous Si features like floating bonds and dangling bonds are displayed in figure 3.4X whereas five, six and seven membered rings are represented in figure 3.4Y with colored dots.....77

Figure 3.5: High-resolution phase-contrast images showing cross-section views of various regions in Au/Cu multilayered thin film **a)** A crystalline Au layer showing nano-twin boundary along with some ordered regions marked as ‘A’ and ‘B’. Interface formed between differently ordered regions consisting of kinks and ledges along the periphery of ‘A’ as shown by solid color lines. **b)** Representation of inter-columnar boundaries as white dotted curves within the crystalline layer of thin film. Ordered regions marked as ‘C’ and ‘D’ display differently ordered interfaces consisting of kinks and ledges as highlighted by solid color lines. Colored arrows show the defects within a grain of Au **c)** high magnification HREM image of the twinned region displaying three differently oriented islands marked as I, II and III. **d)** Representation of the disordered region formed between differently oriented islands. **e)** Region displaying defects just above the twin boundary as marked by solid square in figure 3.5a.80

Figure 3.6: High-resolution phase contrast image (higher magnification version of 3.5(a-b)) showing intermetallic phases grown within the solid solution phase of AuCu with sharp faceted interfaces.83

List of Figures

- Figure 3. 7:** FFT-filtered high-resolution phase contrast images of ordered phases along with their corresponding FFTs (inset) **a)** AuCu (oP8) phase marked as ‘B’ in figure 3.5a **b)** AuCu (oI40) phase marked as ‘C’ in figure 3.5b **c)** AuCu (tP4) phase marked as ‘D’ in figure 3.5b and **d)** Au₃Cu (cP4) phase..... 84
- Figure 3.8:** **a)** Defocus-thickness map for the AuCu (oP8) phase generated by multislice simulation method along $Z = [0\ 1\ 0]$ zone axis. The parameters used in simulation are voltage = 200kV, $C_s = 1.2$ mm and $\Delta f_{Sch} = -65.83$ nm. The close match of simulated image with the experimental image for AuCu (oP8) phase is found at $t \sim 10$ nm and $\Delta f \sim 105$ nm. In the simulation red colour represents Cu and yellow colour represents Au. **b)** Perspective view of unit cell of AuCu (oP8) phase projected along $Z = [0\ 1\ 0]$ direction with upward vector $[2\ 0\ 1]$, **c)** same unit cell projected along $Z = [0\ 1\ 0]$ with upward vector $[4\ 0\ 0]$ 88
- Figure 3.9:** **a)** Defocus-thickness map for the AuCu (oI40) phase generated by multislice simulation method along $Z = [5, 15\ 1]$ zone axis. The parameters used in simulation are voltage = 200kV, $C_s = 1.2$ mm and $\Delta f_{Sch} = -65.83$ nm. The close match of simulated image with the experimental image for AuCu (oI40) phase is found at $t \sim 22$ nm and $\Delta f \sim 150$ nm. **b)** Perspective view of unit cell of AuCu (oI40) phase projected along $Z = [5, 15\ 1]$ direction with upward vector $[1\ 1, 10]$ **c)** same unit cell projected along $Z = [5, 15\ 1]$ with upward vector $[1\ 0\ 5]$ 90
- Figure 3.10:** **a)** Defocus-thickness map for the AuCu (tP4) phase generated by multislice simulation method along $Z = [0\ 1\ 1]$ zone axis. The parameters used in simulation are voltage = 200kV, $C_s = 1.2$ mm and $\Delta f_{Sch} = -65.83$ nm. The close match of simulated image with the experimental image for AuCu (tP4) phase was found at $t \sim 5-7$ nm and $\Delta f \sim 140-145$ nm. **b)** Perspective view of unit cell of AuCu (tP4) phase projected along $Z = [0\ 1\ 1]$ direction with upward vector $[1\ 1\ 1]$ **c)** Same unit cell projected along $Z = [0\ 1\ 1]$ with upward vector $[2\ 0\ 0]$. The contrast arising out as bright spots represents Au and Cu atomic columns..... 91
- Figure 3.11:** **a)** Defocus-thickness map for the AuCu (cP4) phase generated by multislice simulation method along $Z = [1\ 3\ 2]$ zone axis. The

parameters used in simulation are voltage = 200kV, $C_s = 1.2$ mm and $\Delta f_{Sch} = -65.83$ nm. The close match of simulated image with the experimental image for AuCu(cP4) phase is found at $t \sim 10-12$ nm and $\Delta f \sim 130-135$ nm. **b)** Perspective view of unit cell of AuCu (cP4) phase projected along $Z = [1\ 3\ 2]$ direction with upward vector $[1\ 1\ 1]$ **c)** Simulated diffraction pattern of AuCu (cP4) phase along $[1\ 3\ 2]$ zone.....93

Figure 3.12: Schematic representation of the microstructure and interface of the Au/Cu multilayered thin film cross-section.98

Figure 3.13: Schematic representation of the AuCu (oI40) supercell consisting of ten AuCu (tP4) unit cells. Presence of anti-phase boundary with $\langle \frac{1}{2}\ \frac{1}{2}\ 0 \rangle$ translation vector after every five unit cells is indicated by the dotted black line.102

Figure 4.1: Comparison of experimental GIXRD patterns (top two) of Au/Cu multilayer thin films with the simulated patterns of Au-rich (solid solution), Cu-rich (solid solution) and their intermetallics.113

Figure 4.2: Cross-section bright field (BFTEM) image of Au/Cu multilayer thin films **a)** 40TCu specimen and, **b)** 40TAu specimen.115

Figure 4.3: **a)** Cross-section HAADF image of Au/Cu multilayer in 40TCu specimen along with the horizontal scan profile (showing Au and Cu counts), vertical scan profile (showing Au and Cu counts) and, STEM-EDS mapping (showing Au and Cu elemental distribution). **b)** Cross-section HAADF image of Au/Cu multilayer in 40TAu specimen along with the vertical scan profile (showing Au and Cu counts) and, STEM-EDS mapping (showing Au and Cu elemental distribution).117

Figure 4.4: Atomically resolved phase contrast images obtained from the few regions within the multilayer of 40TCu specimen **(a-c)**. Square box ‘1’(orange color) in **(a)**, depicts 2-D lattice fringes. Multislice simulated image of square box ‘1’ along with structure (oP8) overlay is shown in the outset ‘1’. Also, FFT from the same region with its corresponding simulated diffraction pattern and simulated nanocluster (27 unit cells) for oP8 structure is shown alongside. Square box ‘2’(green color) in **(b)**, depicts 2-D lattice fringes. Multislice simulated image of square box ‘1’ along with structure (tP4) overlay is shown in the outset ‘2’. Also, FFT from the same region with its corresponding simulated diffraction pattern and simulated nanocluster (27 unit cells)

List of Figures

- for tP4 structure is shown alongside. Square box ‘3’(cyan color) in (c), depicts 2D lattice fringes. Multislice simulated image of square box ‘3’ along with structure (oI40) overlay is shown in the inset ‘3’. Also, FFT from the same region with its corresponding simulated diffraction pattern and simulated nanocluster (27 unit cells) for oI40 structure is shown alongside. 120
- Figure 4.5:** Schematic representation of the microstructure and interface of the Au/Cu multilayered thin film cross-section of 40TCu specimen. 123
- Figure 5.1:** Schematic representation of the deposition schedule of LiNiO₂ and LiMnO_x on 111 single-crystal Nb-doped SrTiO₃ (Nb:STO) substrate by combinatorial pulse laser deposition..... 133
- Figure 5.2:** (a) Cross-sectional TEM bright-field image of the combinatorially deposited Li(Ni, Mn)_xO_y (LNMO) thin film on 111 single-crystal Nb-doped SrTiO₃ (Nb:STO) substrate (aligned with the experimental diffraction pattern in figure 5.2b. 110 and 111 directions are also marked in the image. 111 is the film growth direction and 110 is parallel to the interface). (b) Electron diffraction pattern from the thin film and the substrate. The substrate is oriented along B= [112] zone axis. (c-e) Simulated electron diffraction patterns of cubic SrTiO₃, cubic LiMn₂O₄ spinel (LMO) and rhombohedral layered LiNiO₂ (LNO) along B= [112], [112], and [210] zone axis respectively. Simulated electron diffraction pattern from (f) cubic LiMn₂O₄ spinel from B = [112], (g) rhombohedral layered LiNiO₂ along B = [210] and, (h) simulated composite electron diffraction pattern from [112] zone axis of cubic LiMn₂O₄ spinel and [210] zone axis of rhombohedral layered LiNiO₂ phase. The blue spots encircled in red represents the unique diffraction spots from spinel for confirmative substantiation of the presence of the spinel phase. Experimentally observed d-spacings are marked on the experimental diffraction pattern. Theoretically expected d-spacings and orientation of reciprocal lattice vectors are marked on the simulated diffraction patterns. Simulated diffraction patterns are not to scale with the experimental diffraction pattern..... 136
- Figure 5.3:** Experimentally observed tilt series diffraction patterns from the thin film around the $\bar{1}\bar{1}1$ reciprocal lattice vector of cubic LiMn₂O₄ spinel (LMO) or $00\bar{3}$ reciprocal lattice vector of rhombohedral layered LiNiO₂

(LNO). Simulated diffraction patterns for cubic LiMn_2O_4 spinel and rhombohedral layered LiNiO_2 along with the orientation of the reciprocal lattice vectors are given for each zone axis. The simulated patterns are to the scale with the experimental patterns. Tilt angles and the ratio of two principal vectors in the diffraction pattern are given. 142

Figure 5.4: (a) HAADF image from the thin film and the substrate, (b) Magnified HAADF image of the thin film and the substrate and (c) the XEDS map of Ni, Mn, Sr and Ti from the thin film and the substrate. (c) XEDS line scan of the constituent elements along the line marked in (a), (d) Low-loss EELS spectra from the thin film obtained in diffraction-coupled mode. 145

Figure 5.5: High resolution phase contrast image from (a) thin film and substrate interface (b) central region of the thin film and (c) top region of the thin film. Nb-doped SrTiO_3 (Nb:STO) substrate was oriented along $B=[112]$ zone axis while imaging (d) FFT from the image in (c), which confirms the presence of the cubic LiMn_2O_4 phase in the film. 147

Figure 5.6: Schematic representation of (a) cubic rock-salt structure (b-c) distortion of cubic rock-salt structure leading to rhombohedral symmetry (d) hexagonal representation of rhombohedral lattice. 149

Figure 5.7: Projection diagram of (a) rhombohedral layered LiNiO_2 (LNO) which is projected along $[210]$ with 001 upward vector and (b) cubic LiMn_2O_4 spinel (LMO) which is projected along $[112]$ with 111 upward vector. 151

Figure 5.8: Simulated Defocus-Thickness map of rhombohedral layered LiNiO_2 (LNO) along $[210]$ by multislice technique. The simulation parameters are $C_s = (-0.00683)$ mm, $A_1 = 0.7246$ nm, $A_2 = 46.68$ nm, $B_2 = 13.8$ nm, $A_3 = 295.3$ nm, $S_3 = 90.35$ nm. In the region of interest (Defocus ~ 23 - 33 nm and thickness ~ 18 - 21 nm) alternating bright and faint fringes are observed. Faint fringes are supposed to be from Li-layer and the relatively bright fringes are from Ni/Mn ions. The oxygen layers are not imaged. 152

Figure 5.9: Simulated Defocus-Thickness map of cubic LiMn_2O_4 spinel (LMO) along $[112]$ by multislice technique. The simulation parameters are $C_s = (-0.00683)$ mm, $A_1 = 0.7246$ nm, $A_2 = 46.68$ nm, $B_2 = 13.8$ nm, $A_3 = 295.3$ nm, $S_3 = 90.35$ nm. For this structure from this zone axis, the atom columns are mostly having mixed chemistry. 153

List of Figures

- Figure 5.10:** Negative aberration-corrected high resolution phase contrast image of $\text{Li}(\text{Ni},\text{Mn})_x\text{O}_y$ thin film in which ordered and disordered regions of rhombohedral layered $\text{Li}(\text{Ni}, \text{Mn})\text{O}_2$ regions and the coherent interface between them are observed. Regions are marked as ‘Layered structure’ and ‘Layer disordering’. Experimental correction parameters are $C_s = (-0.00683)$ mm, $A_1 = 0.7246$ nm, $A_2 = 46.68$ nm, $B_2 = 13.8$ nm, $A_3 = 295.3$ nm, $S_3 = 90.35$ nm. FFTs from the regions ‘1’, ‘2’ and ‘3’ marked by orange, pink and blue windows respectively are given in ‘FFT1’, ‘FFT2’ and ‘FFT3’. The simulated diffraction pattern from rhombohedral layered LiNiO_2 along $B = [210]$ is given by the side of the FFT1. The two dimensional projection of the same structure along $B = [210]$ is given below the FFT2 and FFT3. FFT1 shows complete ordering in rhombohedral layered $\text{Li}(\text{Ni}, \text{Mn})\text{O}_2$, FFT2 shows weak ordering and the FFT3 shows almost no ordering in the same structure. 155
- Figure 5.11:** Negative aberration-corrected high resolution phase contrast image of $\text{Li}(\text{Ni}, \text{Mn})_x\text{O}_y$ thin film in which cubic $\text{Li}(\text{Ni}, \text{Mn})_2\text{O}_4$ spinel and rhombohedral layered $\text{Li}(\text{Ni}, \text{Mn})\text{O}_2$ regions and the coherent interface between them are observed. Experimental correction parameters are $C_s = (-0.00683)$ mm, $A_1 = 0.7246$ nm, $A_2 = 46.68$ nm, $B_2 = 13.8$ nm, $A_3 = 295.3$ nm, $S_3 = 90.35$ nm. FFTs from region ‘1’ and region ‘2’ as marked by orange and blue windows are given as FFT1 and FFT2. The corresponding simulated diffraction patterns overlaid on the FFTs are given just below them. Region ‘1’ matches with cubic LiMn_2O_4 spinel along $B = [112]$ and region ‘2’ matches with rhombohedral layered LiNiO_2 along $B = [210]$ 156
- Figure 5.12:** Negative aberration-corrected high resolution phase contrast image of $\text{Li}(\text{Ni}, \text{Mn})_x\text{O}_y$ thin film in which cubic $\text{Li}(\text{Ni}, \text{Mn})_2\text{O}_4$ spinel, ordered rhombohedral layered $\text{Li}(\text{Ni}, \text{Mn})\text{O}_2$ regions, disordered rhombohedral layered $\text{Li}(\text{Ni}, \text{Mn})\text{O}_2$ regions and the coherent interface between them are observed. Representative regions are marked as ‘Layer structure’, ‘Layer disordering’ and ‘Spinel’. Experimental correction parameters are $C_s = (-0.00683)$ mm, $A_1 = 0.7246$ nm, $A_2 = 46.68$ nm, $B_2 = 13.8$ nm, $A_3 = 295.3$ nm, $S_3 = 90.35$ nm. 158
- Figure 5.13:** Polyhedral representation of (a) rhombohedral layered LiNiO_2 (LNO) and (b) cubic LiMn_2O_4 spinel (LMO) structures. In ordered

rhombohedral layered LiNiO ₂ (LNO) layers of Li ⁺ ions are present between two octahedral layers of oxygen and Ni ions.	165
Figure 6.1: FE-SEM image of the sieved powder after ball milling.	176
Figure 6.2: Multiple display of X-ray diffraction patterns of the powder, ribbon and coating samples.	183
Figure 6.3: (a) Bright field image of the powder, (b) corresponding diffraction pattern of the powder, (c) Bright field image of the ribbon, (d) corresponding diffraction pattern of the ribbon, (e) corresponding dark field image of the ribbon acquired by selecting a part of the ring encircled as shown in the inset, (f) cross-sectional bright field image of the HVOF coated sample, (g) corresponding diffraction pattern of the coated sample, and (h) corresponding dark field image of the coated sample acquired by selecting the spot encircled as shown in the inset.	187
Figure 6.4: (a) Bright field image of the cross-section of the coating, (b) corresponding diffraction pattern of the coating, and (c) simulated diffraction pattern of cF118 (Fe ₁₈ Cr ₆ Mo ₅) structure along [012] zone axis.	190
Figure 6.5: (a) Bright field image of the cross-section of the coating, (b) corresponding diffraction pattern of the coating, and (c) simulated diffraction pattern of oI92 (Fe ₆₂ Cr ₃₄ Mo ₄) structure along [012] zone axis.	191
Figure 6.6: Atomically resolved phase contrast image of the powder specimen. Each square box (1-5) represents variation in phase contrast. Inside the square boxes (1,3,4 and 5), superimposition of their corresponding multislice simulated images is shown. Inset ‘A’ represents the zoomed-in version of the region ‘A’.	193
Figure 6.7: (a) Experimental FFT and simulated diffraction pattern corresponding to square box ‘1’ (figure 6.6) representing oC68 (Fe ₆₂ Cr ₃₄ Mo ₄) structure along [232] zone axis, (b-c) experimental FFT and simulated diffraction pattern corresponding to square box ‘2 and 3’ (figure 6.6) respectively, both represent tP60 (Fe ₆₂ Cr ₃₄ Mo ₄) structure along [121] zone axis (d) experimental FFT and simulated diffraction pattern corresponding to square box ‘4’ (figure 6.6) representing tP58 (Fe ₆₂ Cr ₃₄ Mo ₄) structure along [122] zone axis, (e) experimental FFT and simulated diffraction pattern corresponding to square box ‘5’	

List of Figures

- (figure 6.6) representing mI32 (Fe_5C_2) structure along $[132]$ zone axis, and (f) Stereographic pole figure for the tP30 ($\text{Fe}_{62}\text{Cr}_{34}\text{Mo}_4$) structure along $[122]$ zone axis showing that its structural polymorphs are also oriented along a nearby zone axis..... 195
- Figure 6.8:** (a) Atomic resolution phase contrast image of the oC68 ($\text{Fe}_{62}\text{Cr}_{34}\text{Mo}_4$) structure depicting facets at the interface. The (221) and (202) planes with respect to their relative atomic density are shown alongside, and (b) atomic resolution phase contrast image of the mI32 (Fe_5C_2) structure depicting facets at the interface. The (310) and (112) planes with respect to their relative atomic density are shown alongside..... 198
- Figure 6.9:** Multislice simulated images along with the atoms overlay for (a) oC68 ($\text{Fe}_{62}\text{Cr}_{34}\text{Mo}_4$) (b) tP60 ($\text{Fe}_{62}\text{Cr}_{34}\text{Mo}_4$) (c) tP58 ($\text{Fe}_{62}\text{Cr}_{34}\text{Mo}_4$) and (d) mI32 (Fe_5C_2) structures respectively. 200
- Figure 6.10:** High resolution phase contrast image of the powder specimen. Mark ‘A’ and ‘B’ represent undistorted and distorted regions across the interface. FFT obtained from region ‘A’ is shown along with the simulated diffraction pattern of cI58 structure. The cropped image of region ‘A’ (placed below FFT) is shown along with the multislice simulated image of cI58 structure with atoms overlay. 202
- Figure 6.11:** (a) Zoomed-in image of dotted square box (cyan color) in figure 6.10. Line profiles (1- 5) represent lines (1-5) respectively in (a). 203
- Figure 6.12:** (a) High resolution phase contrast image of the ribbon specimen. Outset 1 represents the magnified version of the cropped region 1 in (a). Multislice simulated image of cI2 ($\alpha\text{-Fe}$) structure is shown alongside outset 1 with overlay of Fe atoms. The (110) plane of the same structure represents the surface with un-bonded Fe atoms. Outset 2 represents the magnified version of the cropped region 2 in (a). Multislice simulated image of oP30 (Fe_2B_7) structure is shown alongside outset 2 with overlay of Fe and B atoms. The relative atomic density associated with the (001) and (820) surface planes of the same structure has also been shown alongside. 204
- Figure 6.13:** Above image shows the surface compositional map through SEM-EDS of single layer coated samples. Uniform distribution of the major alloying elements like ‘Cr’, ‘Mo’, ‘P’ and ‘Si’ was observed in the

coating. Distribution map of ‘O’ shows uniform oxidation at the coated surface.	207
Figure 6.14: Above image shows the elemental map of the coating cross-section obtained by using SEM-EDS across the single layer of coating. Here also uniform distribution of the important alloying elements was observed throughout the coating layer. The elemental map for ‘O’ in the image further substantiates the fact that limited oxidation was observed along the inter-splat boundaries.	208
Figure 6.15: Representation of polyhedrons associated with (a) cF118 ($\text{Fe}_{18}\text{Cr}_6\text{Mo}_5$), (b) oI92 ($\text{Fe}_{62}\text{Cr}_{34}\text{Mo}_4$), (c) oC68 ($\text{Fe}_{62}\text{Cr}_{34}\text{Mo}_4$), (d) tP60 ($\text{Fe}_{62}\text{Cr}_{34}\text{Mo}_4$), (e) tP58 ($\text{Fe}_{62}\text{Cr}_{34}\text{Mo}_4$), (f) mI32 (Fe_5C_2), and (g) oP30 (Fe_2B_7) structures respectively.	210
Figure 6.16: (a) Enthalpy of formation Vs composition curves for amorphous and crystalline phases of Fe-C system, (b) Enthalpy of formation Vs composition curves for amorphous and crystalline phases of Fe-B system, (c) Ternary plot of Fe-Cr-Mo system in which the empty region represents the glass forming composition region. Open colored circles represent the observed crystalline phase compositions in the amorphous matrix. (d) Ternary contour map of Fe-Cr-Mo system representing the value of enthalpy difference between the amorphous and crystalline phase.....	216

LIST OF TABLES

Table 2.1: Details of the Au/Cu multilayer samples.....	40
Table 3.1: Structural parameters used in multislice simulation.....	63
Table 3.2: Calculated crystallize size and average strain from the Au/Cu thin film.	66
Table 3.3a: Comparison of experimentally observed diffraction maxima along with their intensities and d-spacings with the simulated diffraction maxima and intensities for AuCu cF4, and tP4 structures.	67
Table 3.3b: Comparison of experimentally observed diffraction maxima along with their intensities and d-spacings with the simulated diffraction maxima and intensities for AuCu oI40, oP8, and cP4 structures.....	68
Table 3.4: Comparison of the experimentally observed d-spacings from the SAD pattern as shown in figure 3c with the reported d-spacings of the ordered and disordered phases present in AuCu system.	75
Table 5.1: Structural parameters used in multislice simulation.....	135
Table 6. 1: Mild steel composition details.....	177
Table 6.2: Process parameters for High Velocity Oxy Fuel (HVOF) spraying.....	177
Table 6.3a: Structural parameters used in multi-slice simulation cF118, oI92, and oC68 structures.....	180
Table 6.3b: Structural parameters used in multi-slice simulation tP60, tP58, and mI32 structures.....	181
Table 6.3c: Structural parameters used in multi-slice simulation for oP30, cI58, and cI2 structures.....	182
Table 6. 4: d-spacing values corresponding to their (hkl) planes for the observed phases.....	185
Table 6. 5: Details of the phases obtained in the powder, ribbon and coating samples.....	206

ABBREVIATIONS

TEM	:	Transmission Electron Microscope
SEM	:	Scanning Electron Microscope
STEM	:	Scanning Transmission Electron Microscope
HAADF	:	High Angle Annular Dark Field
SAD	:	Selected Area Diffraction
BF	:	Bright Field
DF	:	Dark Field
DCI	:	Diffraction Contrast Imaging
FFT	:	Fast Fourier Transform
XEDS	:	X-ray Energy Dispersive Spectroscopy
EELS	:	Electron Energy Loss Spectroscopy
SEI	:	Solid Electrolyte Interface
NBD	:	Nano Beam Diffraction
HRTEM	:	High Resolution Transmission Electron Microscopy
CTF	:	Contrast Transfer Function
XRD	:	X-ray Diffraction
GI	:	Grazing Incidence
FWHM	:	Full Width Half Maximum
HVOF	:	High Velocity Oxy-Fuel
XTEM	:	Cross-section Transmission Electron Microscopy
MLs	:	Multilayers
NPs	:	Nanoparticles
PLD	:	Pulsed Laser Deposition
LIB	:	Lithium Ion Battery
DI	:	De-ionised
RSP	:	Rapid Solidification Process
BMG	:	Bulk Metallic Glass
BAS	:	Bulk Amorphous Steel

SYMBOLS

θ	:	Bragg angle
λ	:	Wavelength
β	:	Peak brodening
t	:	Crystallite size
ΔH	:	Enthalpy of formation
δ	:	Misfit
ΔG	:	Free energy
d	:	Interplanar spacing
γ	:	Surface energy
a	:	Lattice parameter
ε	:	Bond energy
$^{\circ}$:	Degree
ϵ	:	Strain
k	:	Shape factor

PREFACE

Characterization of surfaces and interfaces in nanostructured materials and thin films is important for understanding functional properties that are vital for electronic and energy applications. The defects such as interphase boundaries, stacking faults, misfit dislocations, anti-phase boundaries are present in nanostructured materials and thin films. Each individual defect type is responsible for the local change of atomic structures in these materials. A little deviation in the atomic structure is bound to change the physical and chemical properties of these materials. Therefore, the atomic structures at and around the surfaces and interfaces play a crucial role in deciding the performance of the microelectronic devices and components. Synthesis of thin films and nanostructured materials mostly lead to the thermodynamically non-equilibrium states of structures at and around interfaces. Additionally, service conditions do change such metastable phases and they transform into various polymorphic states. It is challenging to characterize and understand the origin of such changes in order to tailor the structures, misfits and the kinetics. This study has been taken up with a view to quantitatively characterize the structures, surfaces, interfaces, defects and the chemistry of three material systems 1) metal and alloy, 2) ceramic and, 3) amorphous glass in their nanostructured and thin film states. The investigations have been carried out extensively by using X-ray diffraction (XRD), Grazing incidence XRD (GIXRD), scanning electron microscopy (SEM), transmission electron microscopy (TEM), high resolution TEM (HRTEM), high angle annular dark field (HAADF)-scanning TEM (STEM), X-ray energy dispersive (EDS) and electron energy loss spectroscopy (EELS) techniques coupled with multislice image simulations.

The thesis begins with an introduction (**Chapter 1**) of the surfaces and interfaces, their design, importance, and types. Relevant literatures on surfaces and interfaces have been reviewed briefly. Such an exercise forms the basis to carry out investigation to bridge the

Preface

knowledge gap. This is followed by experimental details (**Chapter 2**). The work carried out as a part of this doctoral work is presented in four subsequent chapters.

Chapter 3 demonstrates the atomic arrangements in the nanostructured grains and interfaces of thermally evaporated Au/Cu multilayer thin films on polycrystalline Si substrate. The same has been explored through GIXRD, HRTEM, simulation, and direct structure imaging. GIXRD pattern conforms to cF4 solid solution of Au and Cu with peak broadening and shift. Comparative analysis with simulation indicated the presence of cP4, tP4, oP8 and oI40 phases in the multilayer. The Cu layer is amorphous. Localized amorphous phase forms at the Cu-Si interface due to the impingement of Cu atoms during deposition. Interfaces of Au/Cu is wavy. The Au layer is polycrystalline and columnar with some twin-like defects present in them. At the Cu/Au interface, diffusionally grown cP4, tP4, oI40 and oP8 phases could be observed. Adatom mobility, concurrent growth and coalescence of growth islands leads to columnar growth. Ordered intermetallic phases could be related with the cF4 solid solution phase through polymorphism. The strain associated with the polymorphs and the solid solution phase is quite small. Faceted semi-coherent interfaces of the ordered phases with the solid solution phase have been resolved. The ordered phases grow into the solid solution matrix by homogeneous transformation. Structure imaging of the ordered phases indicated that most of the time a cluster of atoms is imaged in these structures. The interfaces are likely to be chemically diffused in nature. Polymorphism and homogeneous nature of the transformation at low temperature allows local transformation to ordered phases, that explains the phase field ambiguity in the binary phase diagram. Such structural details are critical in understanding the novel properties in these nanostructured alloys.

Chapter 4 deals with the comparison of the Au/Cu multilayers deposited in two different sequences on the same substrate (Polycrystalline Si). The first one refers to poly-

Si/Cu/Au/Cu/Au and the second one pertains to poly-Si/Au/Cu/Au/Cu. These are respectively designated as 40TAu and 40T Cu. Structural evolution at and around interfaces for sequence 40TAu has been discussed in chapter-3. The comparison of microstructure, interfaces, structural transformations, defects and chemistry of the multilayers has been made on the basis of grazing incidence XRD (GIXRD), transmission electron microscopy (TEM), high resolution TEM (HRTEM), high angle annular dark field (HAADF)-scanning TEM (STEM), X-ray energy dispersive (EDS) results and multislice image simulations coupled with direct structure imaging.

In **Chapter 5**, core-shell $\text{Li}(\text{Ni}, \text{Mn})_x\text{O}_y$ thin film has been deposited onto (111) single-crystal Nb-doped SrTiO_3 (Nb:STO) substrate by pulsed laser deposition. The thin film is ~350-400 nm thick with ~60 nm thick Ni-rich interface. The orientation relationship between the phases and the substrate are $[112]_{\text{STO}} \parallel [112]_{\text{Spinel}}$ and $(\bar{1}\bar{1}1)_{\text{STO}} \parallel (\bar{1}\bar{1}1)_{\text{Spinel}}$; $[112]_{\text{STO}} \parallel [210]_{\text{LiNiO}_2}$ and $(\bar{1}\bar{1}1)_{\text{STO}} \parallel (00\bar{3})_{\text{LiNiO}_2}$; and $[112]_{\text{Spinel}} \parallel [210]_{\text{LiNiO}_2}$ and $(\bar{1}\bar{1}1)_{\text{Spinel}} \parallel (00\bar{3})_{\text{LiNiO}_2}$. The film substrate interface is sharp, non-reactive, free of planar defects. The interfaces between spinel $\text{Li}(\text{Ni}, \text{Mn})_2\text{O}_4$, rhombohedral-layered $\text{Li}(\text{Ni}, \text{Mn})\text{O}_2$, and ordered-disordered domains of are coherent and diffused. As the spacing between octahedral cations in the spinel phase and in the $\text{Li}(\text{Ni}, \text{Mn})\text{O}_2$ phase is different; these two phases could be distinguished by quantifying the spacings between two octahedrally located cations. The electro-chemical behavior of the film is not likely to be optimum with the intended phase composition and chemistry due to disordering in $\text{Li}(\text{Ni}, \text{Mn})\text{O}_2$ phase and unsuitable orientation of the phases. Understanding such structural details is a precursor to tailor the electro-chemical activity in $\text{Li}(\text{Ni}, \text{Mn})_x\text{O}_y$.

Chapter 6 begins with the processing of Fe-based amorphous nanocomposite with nominal composition $\text{Fe}_{58.82}\text{Cr}_{11.12}\text{Mo}_{1.52}\text{Si}_{4.16}\text{B}_{15.12}\text{P}_{8.88}\text{C}_{0.39}$ (at%) through melt-spinning,

Preface

melt-spinning followed by ball milling and thermal spray deposition of coating onto a mild steel substrate. X-ray diffraction and electron microscopy characterization of the processed alloy reveals that the melt-spun ribbon is mostly amorphous with uniform distribution of very fine crystals of α -Fe and oP30 (Fe_2B_7) phase. In the melt-spun followed by ball milled powder mainly cI58 ($\text{Fe}_{18}\text{Cr}_6\text{Mo}_5$), tP30 ($\text{Fe}_{62}\text{Cr}_{34}\text{Mo}_4$) and mI32 (Fe_5C_2) phases are obtained. However, the tP30 ($\text{Fe}_{62}\text{Cr}_{34}\text{Mo}_4$) phase while ball milling undergoes distortive changes locally to produce oC68, tP60 and tP58 phases with similar composition. The interface between the two structures is considerably strained. In the coating, cF118 ($\text{Fe}_{18}\text{Cr}_6\text{Mo}_5$) and oI92 ($\text{Fe}_{62}\text{Cr}_{34}\text{Mo}_4$) are observed in the amorphous matrix. Essentially the cF118 and oI92 can be seen as a structural derivative of cI58 and tP30 phases respectively. Local composition fluctuation and availability of a suitable nucleation condition leads to the nucleation of crystalline phases in the amorphous matrix in the melt-spun ribbon. In the melt-spun followed by ball milled powder further distortive changes are observed locally to form oC68, tP60 and tP58 phases. Even though all the phases are crystallographically quite complicated, they are all derived from either the tP30 ($\text{Fe}_{62}\text{Cr}_{34}\text{Mo}_4$) phase or cI58 ($\text{Fe}_{18}\text{Cr}_6\text{Mo}_5$) phases. Thermodynamic calculations through Miedema's model indicates that the nominal composition of the alloy lies at the boundary of glass forming composition. The crystal compositions, although different from the nominal composition of the alloy, lies in the crystal forming composition range. Local composition fluctuation, favorable thermodynamic conditions for nucleation and growth leads to the crystal nucleation. Although all the phases are crystallographically different, they have similar polyhedral order in them. The polyhedral structures cannot be correlated with Frank-Kasper or Bernal deltahedral phases. This is a significant difference between metal-metalloid glasses with its metal-metal counterpart.

Chapter-7 summarizes the whole study describing the major observations and findings extracted out from the present doctoral work along with the prospects of the future work.

